near enough to the jump epoch to suggest a causal relationship. The data are too noisy to allow the exact time of this phenomenon to be determined, but suggest that it preceded the jump.

The impact of a comet on the neutron star could increase the dispersion measure, leading to the time offset, and could trigger a glitch. We would expect the comet to lose a significant fraction of its mass as it approached the pulsar; much of the mass lost would be ionized and would increase the dispersion measure. The required increase in column density is $\sim 0.016\ \mathrm{cm}^{-3}$ pc, which represents a total mass of $\sim 10^9$ kg if the material is spread in a spherical layer at the light cylinder radius. This is much less than the estimates of cometary masses by Harwit and Salpeter[9] who suggested that γ-ray bursts are the result of cometary impacts on neutron stars. The impact of the comet would cause a local rise in temperature which could trigger the period jump.

An alternative explanation is that the time offset reflects a change in the alignment of the pulsar magnetic field at the epoch of the jump. Such a change may be confined to regions of the magnetic field close to the surface of the pulsar and involve high-order multipole components. Similar non-dispersive phase shifts have been observed in the high-frequency profiles from a number of pulsars, and interpreted in terms of magnetic field restructuring[10].

Data at a third frequency would help to distinguish between these possibilities, and we have added a 1.4-GHz receiver to our 14-m telescope system.

The damped sinusoidal oscillation evident in the post-jump timing residuals is another new feature. A sinusoid in pulsar timing residuals is not uncommon, arising easily as an artefact of the model-fitting procedure. In such cases, however, the parameters of the sinusoid change as the model is varied. Here the damped sinusoid persists as the model is changed, and it also appears in the model-independent plot of $\dot{\nu}$ (Fig. 3). This oscillation, with a period of ~ 25 days, may be the result of a lightly damped Tkachenko oscillation, an axial vibration mode of the lattice of vortex lines in the rotating neutron superfluid[11,12]. The width of the equivalent cylindrical region would need to be ~ 1 km. There is some evidence for a similar low-quality-factor oscillation in the timing residuals before the period jump (Fig. 2). If these are the result of a superfluid oscillation, the parameters should provide further constraints on models of the neutron superfluid in the neutron star. □

Received 23 April; accepted 14 June 1990.

1. McCulloch, P. M., Hamilton, P. A., Royle, G. W. R. & Manchester, R. N. *Nature* **302,** 319–321 (1983).
2. McCulloch, P. M., Klekociuk, A. R., Hamilton, P. A. & Royle, G. W. R. *Aust. J. Phys.* **40,** 725–730 (1987).
3. Flanagan, C. *IAU Circ.* 4695 (1989).
4. Hamilton, P. A., King, E. A., McConnell, D. McCulloch, P. M. *IAU Circ.* 4708 (1989).
5. Manchester, R. N. *et al. Mon. Not. R. astr. Soc.* **184,** 159–170 (1978).
6. Hamilton, P. A., Hall, P. J. & Costa, M. E. *Mon. Not. R. astr. Soc.* **214,** 5P–7P (1985).
7. Baym, G., Pethick, C., Pines, D. & Ruderman, M. *Nature* **224,** 872–874 (1969).
8. Alpar, M. A., Anderson, P. W., Pines, D. & Shaham, J. *Astrophys. J.* **278,** 791–805 (1984).
9. Harwit, M. & Salpeter, E. E. *Astrophys. J.* **186,** L37–L39 (1973).
10. Kuzmin, A. D., Malofeev, V. M., Izvekova, V. A., Sieber, W. & Wielebinski, R. *Astr. Astrophys.* **161,** 183–194 (1986).
11. Ruderman, M. *Nature* **225,** 619–620 (1970).
12. Sonin, E. B. *Rev. mod. Phys.* **59,** 87–155 (1987).

Fingering instability of thin spreading films driven by temperature gradients

A. M. Cazabat, F. Heslot, S. M. Troian* & P. Carles

Physique de la Matière Condensée, Collège de France,
11 place Marcelin Berthelot, 75231 Paris Cedex 05, France

THE dynamics of spreading of thin liquid films are important to many technological and biological processes, including tertiary oil recovery, coating processes, the formation and protection of microchips and biological cell interactions. The spontaneous spreading of thin liquid films under capillary forces alone is typically a slow process. An applied force—gravitational or centrifugal, or a surface shear stress—can be used to drive the spreading more quickly[1,2]. Recent experimental[3,4] and theoretical[5] studies have revealed that in all of these cases of forced spreading, the liquid front undergoes a fingering instability. Here we report another example of such unstable driven flow, this time caused by the Marangoni effect[6], in which a temperature gradient induces a gradient of surface tension which drives the spreading process.

Thin films of liquids can be made to rise above the equilibrium meniscus position under the force of an upwardly directed gradient in the surface tension[2]. Such Marangoni films are formed by applying a thermal gradient along a vertical surface, which gives rise to a surface tension gradient along the direction of flow, $\mathrm{d}\gamma/\mathrm{d}x = (\mathrm{d}\gamma/\mathrm{d}T)(\mathrm{d}T/\mathrm{d}x)$, where γ is the local surface tension, T the local temperature and x the vertical distance along the plate. The temperature variation of the surface tension, $(1/\gamma)(\mathrm{d}\gamma/\mathrm{d}T)$, is fairly constant for many fluids far from the critical point, and therefore a constant temperature gradient creates a constant Marangoni surface stress $\tau = \mathrm{d}\gamma/\mathrm{d}x$. In the lubrication approximation, the Navier–Stokes equations describing such unidirectional flow reduce to

$$\eta \frac{\partial^2 v}{\partial z^2} = \frac{\partial p}{\partial x} + \rho g \tag{1}$$

where $v(x, z)$ is the fluid velocity upwards along the plate, z is the distance from the solid, η is the viscosity, p is the pressure in the fluid, and ρg the gravitational force per unit volume. For very thin films, $\rho g \ll \partial p/\partial x$, and for small surface curvature $\partial p/\partial x = -\gamma(\mathrm{d}^3 h/\mathrm{d}x^3)$, where $h(x)$ defines the film surface. (To first order, one can ignore the temperature dependence of the viscosity, which induces higher-order effects than we investigate here, as well as the variation of surface tension in the pressure-gradient term.) Integrating equation (1) subject to the boundary conditions $v(x, z=0) = 0$ and $\eta(\partial v/\partial z)(z = h(x)) = \tau$ gives the height-averaged velocity

$$V(x) = \frac{h}{2\eta}\tau + \frac{\gamma}{3\eta} h^2 \frac{\mathrm{d}^3 h}{\mathrm{d}x^3} \tag{2}$$

The first term describes the climbing of the film under Marangoni forces (for τ positive), and the second term describes flow induced by surface curvature (Laplace pressure). Away from the sharply curved ends of the meniscus region near the bottom of the plate and the advancing front, the surface curvature is negligible and the fluid velocity is dominated by the first term. Under quasistatic conditions in which the incoming flux, $Q = hV$, is constant, $h(x)$ will be nearly flat and the fluid film should spread linearly in time with a constant velocity V_{th} given by

$$V_{\mathrm{th}} = \frac{h_0 \tau}{2\eta} \tag{3}$$

where h_0 is the thickness of the flat film. This thickness is determined by both the detailed fluid geometry in the meniscus region and by the magnitude of the thermal stress pulling the film up along the wafer. h_0 can be found by asymptotically matching the height profile from the Maragoni-driven region to the height profile determined from the menisicus region in which

* Permanent address: Exxon Research and Engineering Corp., Clinton Twp., Route 22E, Annandale, New Jersey 08801, USA.

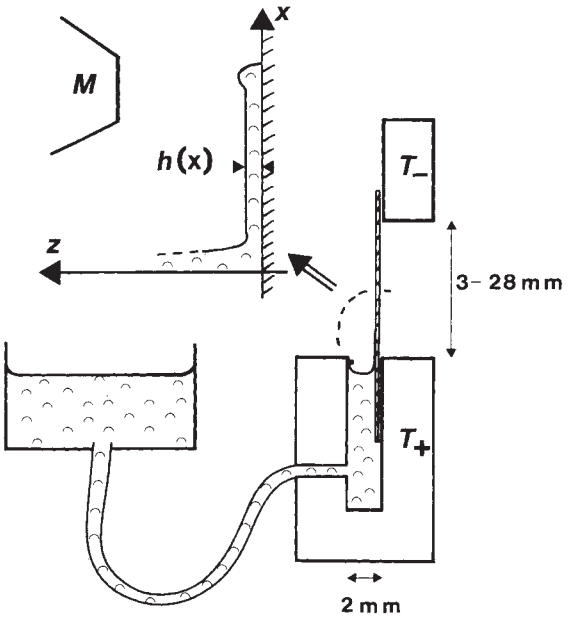

FIG. 1 A schematic of the capillary rise geometry. Upper left-hand corner shows a magnified view of the meniscus region.

only gravitational and capillary forces matter. This requires a knowledge of the specific boundary conditions near the injection site in the meniscus region. We need not solve explicitly for h_0 in the analysis which follows.) The capillary contribution to the velocity becomes important near the advancing front where the fluid surface curves sharply to meet the substrate. Balancing the two terms in equation (2) gives that the length L, near the moving front, over which the capillary force is comparable to the viscous and Marangoni forces is

$$L = h_0(3\,\mathrm{Ca})^{-1/3} \qquad (4)$$

where the capillary number is $\mathrm{Ca} = \eta V_{\mathrm{th}}/\gamma$. As first suggested by Huppert[3] and calculated explicitly in ref. 5, the length of this capillary region is what determines the wavelength Λ of the fingering instability, a result we confirm below.

TABLE 1 Dependence of spreading on viscosity and temperature gradient

η (mPa s)	τ (N m^{-2})	h_0 (μm)	V_{exp} (μm s^{-1})	Λ (μm)	V_{th} (μm s^{-1})	L (μm)	Λ/L
20	0.5	0.86	8*	600	10.7	27	22
20	0.27	0.65	3*	610	2.8	27	22
20	0.21	0.54	3	480	2.8	25	19
20	0.10	0.27	1	370	0.68	20	18
20	0.054	0.17	0.3	340	0.23	18	19
100	0.21	0.65	0.8	580	0.7	28	21
500	0.21	0.33	0.1†	340	0.07	18	19

* Linear regime too short or † slope not sufficiently constant to give a precise reading.

We have studied the climbing rate of films of a light silicone oil polydimethylsiloxane (PDMS, Petrarch Systems) on oxide-covered silicon wafers in a capillary-rise geometry as shown in Fig. 1. The wafers are cleaned with hexane, then methanol, providing a surface completely wettable by PDMS. The 250-μm-thick wafers are held vertical by aspiration against two mobile brass blocks kept at a constant temperature difference of 28 °C (top block colder). We estimate the surface tension gradient in the film by calculating the temperature gradient along the wafer (28 °C divided by the distance between the blocks).

Fluid enters the system through a plastic tube connecting the reservoir bottle and the pool of liquid in which the bottom edge of the wafer is dipping. The temperature gradient is first established with the wafer in position; then the level of fluid is slowly raised (by moving the reservoir bottle) to where the fluid meniscus on the wafer just reaches into the thermal gradient region.

The climbing film is observed through a reflection microscope with laser illumination ($\lambda = 6{,}328$ Å). Equal-thickness fringes, spaced $\lambda/2n$ apart (where $n = 1.4$ is the optical index of the PDMS), are used to reconstruct the thickness profiles. Figure 2 *a–d* shows the typical development of a film spreading under a temperature gradient. The spurious vertical interference lines correspond to fringes from a half-silvered mirror inclined at 45° in the microscope and used for illumination. Some time after the liquid is put into contact with the vertical wafer (the time delay depending on the fluid viscosity and the magnitude of the temperature gradient), a film of relatively constant thickness begins climbing the wafer (Fig. 2*a*). A bump in the height profile,

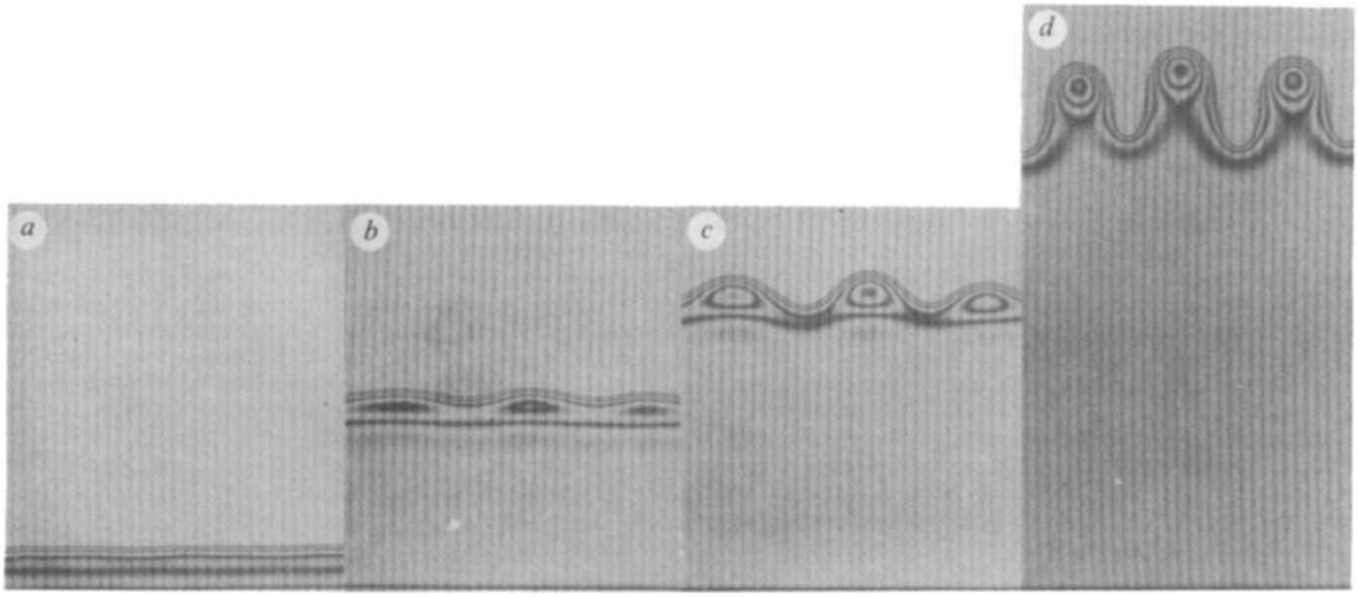

FIG. 2 Time development of the fingering instability at the vertically ascending front of a PDMS oil film of 20 mPa s^{-1} and $\tau = 0.18$ Pa. *a*, 1.5 min; *b*, 6.5 min; *c*, 10 min; *d*, 17 min. Measured from tip to tip, the wavelength Λ in *d* is 0.5 mm.

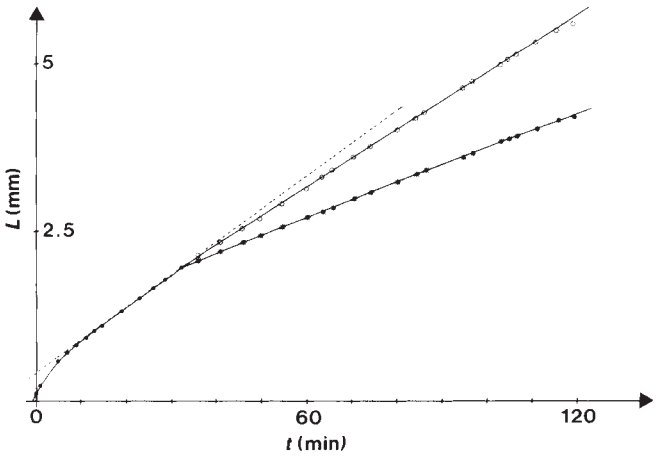

FIG. 3 Position of the fluid front as a function of time for PDMS of 100 mPa s^{-1} and $\tau = 0.21$ Pa. The values V_{exp} in Table 1 are determined from the slope of the linear regime occurring before the onset of the instability.

indicated by the closely spaced fringes near the front of the film, develops near the climbing front (Fig. 2*b*), which soon becomes unstable (Fig. 2*c*) and results in a fingering instability with a rather well defined wavelength (Fig. 2*d*). Figure 3 shows the position of the fluid front as a function of time. The fork in the curve signals the beginning of the instability, the upper curve corresponding to the finger tips and the bottom one to the 'valley'. After some initial transients, but before the onset of the instability, the front moves linearly in time, as predicted for a film of constant height. Once the instability has developed, both the tips and valleys also grow linearly in time. Not surprisingly, the linear development for the finger growth is different both from that for gravitational[3] and for rotational flow[4] because of the absence of constant fluid volume and different flow geometry (linear instead of radial) in our case.

For more detailed comparison between the predicted and measured values of the film velocity without the fingers and of the wavelength of the instability, we used silicone oils of varying viscosity and applied several different temperature gradients as shown in Table 1. The quantities h_0 and V_{exp} are experimentally measured values. Λ is the measured wavelength of the instability, and V_{th} and L were calculated using equations (3) and (4). For the oils used, the surface tension, $\gamma = 20$ mN m^{-1}, does not vary much with molecular weight, and $|(1/\gamma)(d\gamma/dT)| = 0.0025$ K^{-1}. In evaluating the capillary number, we used the viscosities of the fluids at 25 °C. The agreement between the measured and predicted values of the velocity is quite good.

The height profiles in the absence and presence of the instability as well as the growth rate of the instability as a function of wavenumber have been calculated in a linear stability analysis (E. Herbolzheimer and S. M. Troian, manuscript in preparation). A detailed comparison of the predicted and measured height profiles will be published elsewhere, but this analysis shows that the pronounced bump observed in the height profile causes a capillary-driven fingering instability more complex yet not unlike the Rayleigh instability (the breakup of a liquid column into droplets). In our case, one can think of the bump as a long roll of fluid (in the y direction) the axial symmetry of which is broken by liquid being pumped in from the back. The bump forms because the contact line cannot move as fast as the fluid being pumped in from behind by the Marangoni stress. When the bump or roll develops enough axial curvature, the timescale depending on the thermal gradient and the liquid viscosity, the roll becomes unstable and breaks up into fingers. If the mode observed is the one with the fastest-growing wavelength, the theoretical ratio of $\Lambda/L = 25$ is in good agreement with the average measured value of 20 (Table 1). □

Received 17 April; accepted 16 July 1990.

1. Tanner, L. H. *La Recherche* **17,** 182–191 (1986).
2. Ludviksson, V. & Lightfoot, E. N. *Am. Inst. Chem. Engrs J.* **17,** 1166–1173 (1971).
3. Huppert, H. E. *Nature* **300,** 427–429 (1982).
4. Melo, F., Joanny, J. F. & Fauve, S. *Phys. Rev. Lett.* **63,** 1958–1961 (1989).
5. Troian, S. M., Herbolzheimer, E., Safran, S. A. & Joanny, J. F. *Europhys. Lett.* **10,** 25–30 (1989).
6. Levich, V. G. & Krylov, V. S. *A. Rev. Fluid Mech.* **1,** 293 (1969).

Significant flux of atmospheric nitrous oxide from the northwest Indian Ocean

C. S. Law & N. J. P. Owens

Plymouth Marine Laboratory, Prospect Place, The Hoe, Plymouth, Devon PL1 3DH, UK

INTEREST in nitrous oxide (N_2O) has increased considerably in the light of its deleterious effect on the ozone layer[1], and contribution to the greenhouse effect[2]. There are many sources of atmospheric N_2O, both anthropogenic (for example, combustion) and natural, but the global budget is still inadequately defined. Despite the fact that most of the world's oceans are close to equilibrium with the atmosphere[3], water bodies depleted in oxygen have been identified as areas of N_2O production[4,5], and so the oceans represent a potential source of atmospheric N_2O. Here we report elevated N_2O concentrations in the northwest Indian Ocean, an area that exhibits upwelling and high oxygen consumption in the water column. We found that N_2O was supersaturated in both oxygen-saturated surface waters (up to 246% N_2O saturation) and oxygen-depleted sub-surface waters (1,264% N_2O saturation). The calculated flux to the atmosphere indicated that upwelling in the northwest Indian Ocean (15–25° N) represents one of the most significant marine sources of N_2O, contributing between 5 and 18% of the total marine flux from a surface area of only 0.43% of the world ocean. These data suggest that the oceanic flux of N_2O to the atmosphere shows strong spatial heterogeneity which should be considered in global budgets and ocean–atmosphere models.

A transect of the northwest Indian Ocean (Fig. 1) was followed from close to the Equator (00°04′ N 65°05′ E), across the Arabian Sea into the Gulf of Oman (24°49′ N 57°13′ E) during September–October 1986. Vertical profiles of dissolved N_2O (and other oceanographic variables) were obtained at 16 stations by sampling at 20–24 depths between the surface and 4,000 m. This region exhibits two important oceanographic features: (1) a monsoon-driven upwelling, located off the Arabian Peninsula; (2) sub-surface waters that are persistently severely depleted in oxygen[6]. The upwelling is dominant during June–August when the southwesterly winds average 10–11 m s^{-1}; whereas the rest of the year is characterized by a mean wind speed of 4 m s^{-1} (Meteorological Office, Bracknell, UK) with reduced upwelling. The water column was generally supersaturated with N_2O with respect to an atmospheric N_2O concentration of 303.9 parts per 10^9 by volume (ref. 3, with subtraction of 0.2% to account for the annual increase in atmospheric N_2O); the data are therefore considered in terms of ΔN_2O, which represents the excess N_2O over that which would be in equilibrium with the atmosphere. Dissolved oxygen concentrations are presented in terms of the apparent oxygen utilization, AOU (the difference between the equilibrium oxygen concentration at ambient temperature and salinity and the observed oxygen concentration), which is a measure of the degree of oxygen depletion.

Figure 1 shows the N_2O–depth distribution from stations 1 to 11. All profiles exhibited a similar trend with an increase in ΔN_2O between 200 and 1,000 m, coincident with the oxygen minimum. ΔN_2O maxima of >45 nmol l^{-1} were recorded in the upwelling region (stations 6–16), and also at station 3 where lower-salinity surface water, originating from the region of the